Earth and Planetary Science Letters 579 (2022) 117368

Contents lists available at ScienceDirect

Earth and Planetary Science Letters

www.elsevier.com/locate/epsl

Global and local drivers of the Ediacaran Shuram carbon isotope excursion

James F. Busch [a,*], Eben B. Hodgin [b], Anne-Sofie C. Ahm [c,d], Jon M. Husson [d], Francis A. Macdonald [e], Kristin D. Bergmann [f], John A. Higgins [c], Justin V. Strauss [a]

[a] Dartmouth College, Department of Earth Sciences, Hanover, NH 03755, USA
[b] University of California, Berkeley, Earth and Planetary Sciences, Berkeley, CA 94720, USA
[c] Princeton University, Department of Geosciences, Princeton, NJ 08540, USA
[d] University of Victoria, School of Earth and Ocean Sciences, Victoria, BC, Canada
[e] University of California, Santa Barbara, Department of Earth Sciences, Santa Barbara, CA 93106, USA
[f] Massachussetts Institute of Technology, Department of Earth, Atmospheric, and Planetary Sciences, Cambridge, MA 02139, USA

ARTICLE INFO

Article history:
Received 2 September 2021
Received in revised form 1 January 2022
Accepted 5 January 2022
Available online xxxx
Editor: B. Wing

Keywords:
Shuram excursion
Ediacaran
diagenesis
carbonate geochemistry

ABSTRACT

The Ediacaran Shuram carbon isotope excursion (CIE) follows the regional Gaskiers glaciation and occurs before the appearance of macroscopic animal fossils. Previous interpretations for the Shuram CIE have proposed global perturbations to Earth's carbon cycle accompanied by significant climatic and environmental change. These studies assume that carbonate carbon isotopes through the Shuram CIE record the composition of dissolved inorganic carbon in seawater. Through a compilation of new geochemical, sedimentological, and stratigraphic data from five localities on four separate paleocontinents, we find that all of the analyzed Shuram CIE successions share general similarities including a common transgressive-regressive sequence that is coincident with similar shifts in a host of geochemical proxies ($\delta^{13}C$, $\delta^{18}O$, $\delta^{44/40}Ca$, Sr/Ca, Mn/Sr, U/Ca). Despite these broad similarities between sections, there are important differences in the proxies between water depths that may be linked to changes in carbonate diagenesis. Specifically, we find the excursion's magnitude is largest in slope environments where diagenesis is sediment-buffered and smaller in shallow-water settings dominated by fluid-buffered diagenesis. The transgression that accompanied the Shuram CIE is consistent in amplitude (~10-100s m) and duration (>1 My) with eustatic fluctuations driven by plate reorganization. These coupled geochemical and stratigraphic observations argue against meteoric and burial diagenesis as drivers for the excursion; instead, they are best explained by global changes to the locus and intensity of photosynthetic primary productivity in shallow-water environments and do not necessarily require large changes in global climate or marine redox.

© 2022 Elsevier B.V. All rights reserved.

1. Introduction

Negative carbonate carbon isotope ($\delta^{13}C$) values below the canonical mantle input value of ~−5‰, such as those that characterize multiple Neoproterozoic carbon isotope excursions (CIEs) (e.g., Halverson et al., 2010), are not easily explained through changes to the fraction of organic to total carbon burial in a steady state carbon cycle. Recent models have instead invoked non-steady state behavior, diagenesis, disconnection from open ocean DIC, and methane release to explain these phenomena (e.g., Ahm et al., 2021, 2019; Bjerrum and Canfield, 2011; Knauth and Kennedy, 2009; Rothman et al., 2003; Schrag et al., 2013).

The Shuram is the largest CIE in the geological record and has been documented worldwide (Fig. 1; Grotzinger et al., 2011). Radioisotopic age constraints support correlations between the Shuram CIE on multiple paleocontinents (Rooney et al., 2020), but ambiguity still exists in correlating other Ediacaran excursions (Hay et al., 2019; Rooney et al., 2020; Yang et al., 2021). The chemostratigraphic expression of this excursion is marked by pre-Shuram $\delta^{13}C$ values as high as +10‰, nadir values as low as −15‰, a lack of covariation between organic and carbonate $\delta^{13}C$ values, and strong covariation between carbonate $\delta^{13}C$ and $\delta^{18}O$ values (Derry, 2010; Grotzinger et al., 2011). In addition to its magnitude, previous attempts to correlate and identify similarities among Shuram

* Corresponding author.
E-mail address: james.f.busch.gr@dartmouth.edu (J.F. Busch).

https://doi.org/10.1016/j.epsl.2022.117368
0012-821X/© 2022 Elsevier B.V. All rights reserved.

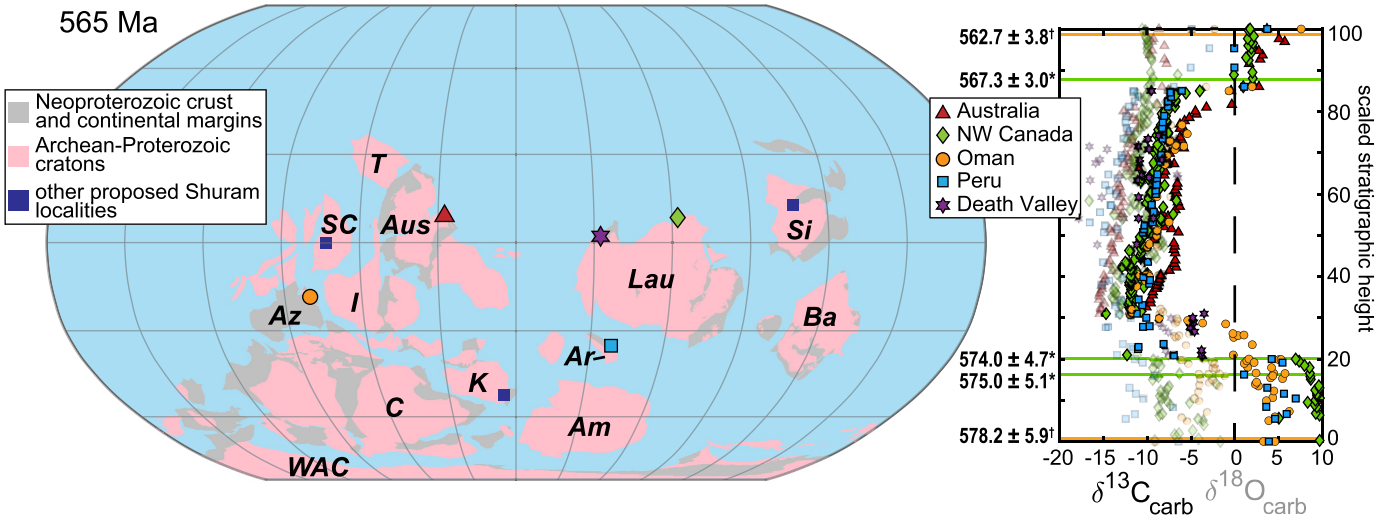

Fig. 1. Paleogeographic reconstruction at the ca. 565 Ma termination of the Shuram CIE after Merdith et al. (2021) and marine carbonate $\delta^{13}C$ and $\delta^{18}O$ profiles for the locations included in this study. Am, Amazonia; Ar, Arequipa; Aus, Australia; Az, Azania; Ba, Baltica; C, Congo; I, India; K, Kalahari; Lau, Laurentia; SC, South China; Si, Siberia; T, Tarim; WAC, West African Craton. *NW Canada Re-Os date (Rooney et al., 2020); †Oman Re-Os date (Rooney et al., 2020).

CIE-bearing successions have emphasized several defining characteristics: 1) stratigraphic position above ca. 635 Ma Marinoan cap dolostones but below the ca. 560–549 Ma White Sea Ediacaran faunal assemblage; 2) stratigraphic asymmetry marked by a sharp downturn to negative values, which is often missing, and a gradual return back to 0‰; 3) small point-to-point difference between isotope ratios of consecutive samples; 4) stratigraphic expression over 10's to 100's of meters of measured section; and 5) development within a transgressive sequence (Bergmann et al., 2011; Burns and Matter, 1993; Grotzinger et al., 2011; Rooney et al., 2020). In addition, the Shuram CIE has been associated with the ca. 580 Ma Gaskiers glaciation and the ca. 571 Ma first appearance datum (FAD) of the Avalon fossil assemblage, fueling speculation around a connection between these geobiological events (e.g., Grotzinger et al., 2011); however, recent geochronological data from Northwest Canada, Oman, and Newfoundland demonstrate the CIE postdates both the Gaskiers glaciation and the Avalon assemblage FAD (Canfield et al., 2020; Matthews et al., 2020; Rooney et al., 2020).

In this study, we attempt to provide additional paleoenvironmental context for the Shuram CIE through a compilation of new geochemical and sedimentological data from five localities across four paleocontinents (Fig. 1). In particular, we seek to leverage the newly developed framework for deconvolving the effects of mineralogy and early marine diagenesis on the paleoenvironmental information preserved in carbonate rocks using paired measurements of $\delta^{44/40}Ca$ and $\delta^{26}Mg$ values and trace elements (Sr/Ca, Mn/Sr; Higgins et al., 2018). Measurements of the calcium isotopic composition of Shuram-bearing carbonate rocks also provide an opportunity to test whether strata from different paleocontinents are representative of the average global carbonate sink, as would be expected if the Shuram CIE was a large globally synchronous perturbation to the carbon cycle (e.g., Rothman et al., 2003).

2. Materials and methods

Detailed measured sections from each study location were compiled and interpreted in a transgressive-regressive (T-R) sequence stratigraphic framework. Relative water depth was extrapolated from inferred depositional environments and diagnostic sedimentary structures. Geochemical data compiled for this study are primarily unpublished but also include data reported in Husson et al. (2015a) and Bergmann (2013). The data include $\delta^{13}C$ ($n = 951$), $\delta^{18}O$ ($n = 951$), $\delta^{44/40}Ca$ ($n = 680$), and $\delta^{26}Mg$ ($n = 227$) isotopic measurements, in addition to Mg/Ca, Sr/Ca, Mn/Ca, U/Ca major, and trace elemental ratios ($n = 783$) (Supplemental S1). The reader is referred to Supplemental S2 for sample preparation and laboratory methodologies.

3. Geological background

Data was collected from five localities on four different paleocontinents (Fig. 1): (1) Flinders and Gammon Ranges of South Australia; (2) Wernecke and Ogilvie Mountains of Northwest Canada; (3) Ibex and Saddle Peak hills of Death Valley, USA; (4) South Oman Salt Basin and Huqf Outcrop areas of Oman; and (5) the Marcona region of southwestern Peru. Detailed information on the regional geology and stratigraphy/sedimentology of each study location is presented in Supplemental S3, with the descriptions below focused on gross stratigraphy and lithofacies.

3.1. South Australia

In Australia, siliciclastic rocks of the Bunyeroo Formation (Fm) are conformably overlain by ~100 m of mixed siliciclastic-carbonate strata (units 1-3) of the lower Wonoka Fm, which records a $\delta^{13}C$ nadir of −12‰ (Husson et al., 2015a, 2015b). The overlying ~650 m of the Wonoka Fm (units 3-8) record $\delta^{13}C$ values that gradually change back towards 0‰. Post-CIE units 9-11 of the Wonoka Fm are ~150 m thick and record a return to positive $\delta^{13}C$ values up to +6‰ in mixed siliciclastic-carbonate facies before an upper contact with the Pound Subgroup (Husson et al., 2015a, 2015b).

3.2. Northwest Canada

In Northwest Canada, mixed siliciclastic-carbonate strata of the ca. 574 Ma Nadaleen Fm and Gladman member of the Last Chance Fm contain positive $\delta^{13}C$ values up to +10‰ and are overlain by the CIE-bearing Gametrail and Last Chance formations of the Rackla Group with nadir $\delta^{13}C$ values reaching −15‰ (Busch et al., 2021; Macdonald et al., 2013; Moynihan et al., 2019; Rooney et al., 2020). A return to 0‰ is recorded in the upper Gametrail Fm across a karstic unconformity in shallow-water locations of the Wernecke Mountains and across a major facies change in the ca. 567 Ma Fireweed member of the Last Chance Fm of the Ogilvie

Mountains, which is marked by positive $\delta^{13}C$ values up to +5‰. In the distal Nadaleen River region of the Wernecke Mountains, a transition to positive $\delta^{13}C$ values up to +2‰ occurs in mixed siliciclastic-carbonate facies of the upper Gametrail Fm, which is overlain by the siliciclastic-dominated Blueflower Fm (Moynihan et al., 2019).

3.3. Peru

In Peru, the CIE-bearing San Juan Fm (Chew et al., 2007) is divided into three informal members (units SJ1, SJ2, and SJ3) (Hodgin, 2020). Pre-CIE carbonate strata of unit SJ1 that contain positive $\delta^{13}C$ values up to +8‰ are conformably overlain by mixed siliciclastic-carbonate strata of unit SJ2, which captures the CIE with a nadir of −11‰. The post-CIE recovery to positive $\delta^{13}C$ values up to +4‰ occurs in carbonate of the overlying SJ3 unit (Chew et al., 2007; Hodgin, 2020).

3.4. Oman

Outcrop exposures of the Khufai Fm in the Huqf area have positive $\delta^{13}C$ values up to +6‰ that decrease towards its upper contact with the Shuram Fm (Bergmann, 2013; Le Guerroué et al., 2006; Osburn et al., 2015). Highly negative $\delta^{13}C$ values with a nadir of −12‰ are recorded within mixed siliciclastic-carbonate strata of the lower Shuram Fm, and gradually return to 0‰ over a thickness of ∼400 m into overlying carbonate strata of the lower Buah Fm. The upper Buah Fm is characterized by positive $\delta^{13}C$ values up to +7‰ (Bergmann, 2013; Le Guerroué et al., 2006).

3.5. Death Valley

In Death Valley, pre-CIE siliciclastic-dominated strata of the Johnnie Fm are divided into five members (Stewart, 1970). The downturn of the CIE is recorded at the base of the uppermost member of the Johnnie Fm, the Rainstorm Member, in the ∼2 m thick "Johnnie oolite" marker bed (e.g., Bergmann et al., 2011). The CIE nadir of −11‰ and return towards 0‰ occur in mixed siliciclastic-carbonate strata of the upper Johnnie Fm over a thickness of ∼100 m before its contact with the overlying Stirling Fm (Bergmann et al., 2011; Summa, 1993; Verdel et al., 2011).

4. Results

4.1. Sedimentological and stratigraphic expressions of the Shuram CIE

The CIEs preserved in Ediacaran sections described above are correlated and referred to below as Shuram CIEs. Ediacaran sedimentary lithofacies are distinct between pre-, syn-, and post-Shuram intervals and reflect marine sedimentation over a range of water depths between upper slope and inner ramp depositional environments (Figs. 2, 3).

4.1.1. Pre-Shuram CIE

In Peru and Oman, pre-Shuram CIE strata are characterized by stromatolitic boundstone and oolitic grainstone. In contrast, the uppermost pre-Shuram strata in Death Valley, Northwest Canada, and Australia are largely siliciclastic-dominated units composed of interbedded mudstone, siltstone, and sandstone. At the top of each of these sub-Shuram successions, there is a prominent sequence boundary (Fig. 2B-C, 3). In Australia, the sequence boundary is represented by a prominent shift from hummocky cross-stratified sandstone and calcareous siltstone of unit 2 to a generally finer-grained package of interbedded siltstone and fine-grained limestone in unit 3 of the Wonoka Fm, while in Peru and Oman there is a sharp shift from shallow-water carbonate to deep-water fine-grained mixed siliciclastic-carbonate lithofacies (Fig. 3). In Northwest Canada, proximal locations contain evidence for a subaerial exposure surface at this boundary (Fig. 2B), while distal localities record a sharp change from siliciclastic to carbonate lithofacies (Fig. 3). In Death Valley, the base of the Johnnie oolite marker bed is associated with a prominent sequence boundary (Fig. 2C).

4.1.2. Syn-Shuram CIE

These sub-Shuram sequence boundaries are accompanied by an abrupt shift to mixed siliciclastic-carbonate strata that are remarkably similar on each paleocontinent (Fig. 2D-F, 3). Above the downturn of the excursion (where present), basal syn-Shuram strata consist predominantly of pink to gray fine-grained silty lime mudstone and/or dolomudstone characterized by hummocky cross-stratification, abundant intraclast rudstone, and rare aragonite crystal fan pseudomorphs (Fig. 2F). This distinct facies assemblage is common to all of the syn-Shuram rocks independent of depositional setting (Fig. 2D-F), and the fine-grained siliciclastic component is notable in strata that are otherwise pure carbonate. Strata overlying the Shuram nadir in Australia, as well as distal locations in Northwest Canada and Oman, record a conspicuous interval of maroon-colored turbiditic silty limestone with abundant flute and gutter casts (Fig. 2D, E). In Australia, Oman, and Peru, the silt content of these nadir strata decreases gradationally up-section (Fig. 3).

4.1.3. Post-Shuram CIE

Post-Shuram strata from all these localities also record a similar facies shift (Fig. 3), with the boundary between syn- and post-Shuram strata marked by another prominent sequence boundary. In Australia, this sequence boundary is marked by the abrupt appearance of interbedded cross-stratified calcareous sandstone and doloboundstone (Fig. 2G). In the proximal locations of Northwest Canada, there is a subaerial exposure surface characterized by paleokarst cavities that extend over ∼6 m deep into the underlying strata (Fig. 2H); in distal locations, there is an influx of coarse-grained siliciclastic detritus into the carbonate-dominated slope facies (Fig. 3). In Oman, the post-Shuram sequence boundary is marked by transgressive stromatolitic buildups (Fig. 3). In Peru, the sequence boundary marks a shift to thin- to medium-bedded dolograinstone, intraclast dolorudstone, and recrystallized dolostone (Fig. 3). In Death Valley, the upper sequence boundary is characterized by an erosional unconformity marked by paleocanyons that locally incise into underlying strata and contain sedimentary breccia with blocks up to 15 m in size (Fig. 2I; Clapham and Corsetti, 2005). These paleocanyon fills are disconformably overlain by the Stirling Fm (Fig. 3).

4.1.4. Inferred depositional settings

Based upon the facies associations reviewed above (also see Supplemental S3), pre-Shuram strata in Oman are interpreted to represent peritidal to subtidal carbonate depositional environments, and in Peru they are interpreted to broadly represent inner ramp settings. In contrast, the pre-Shuram strata of Australia and Death Valley are interpreted to record middle to outer ramp depositional environments. In Northwest Canada, proximal locations capture inner to outer ramp sedimentation while distal locations record slope settings. The basal Shuram-bearing strata across all these disparate regions are interpreted to record a significant flooding event and contain evidence for deposition under storm-dominated conditions. This transgressive event locally floods inner ramp environments, such as those recorded in Oman and Peru, placing most of the studied locations into middle to outer ramp or slope settings throughout the duration of the Shuram CIE. The peak transgression in most of these successions (referred to here as the

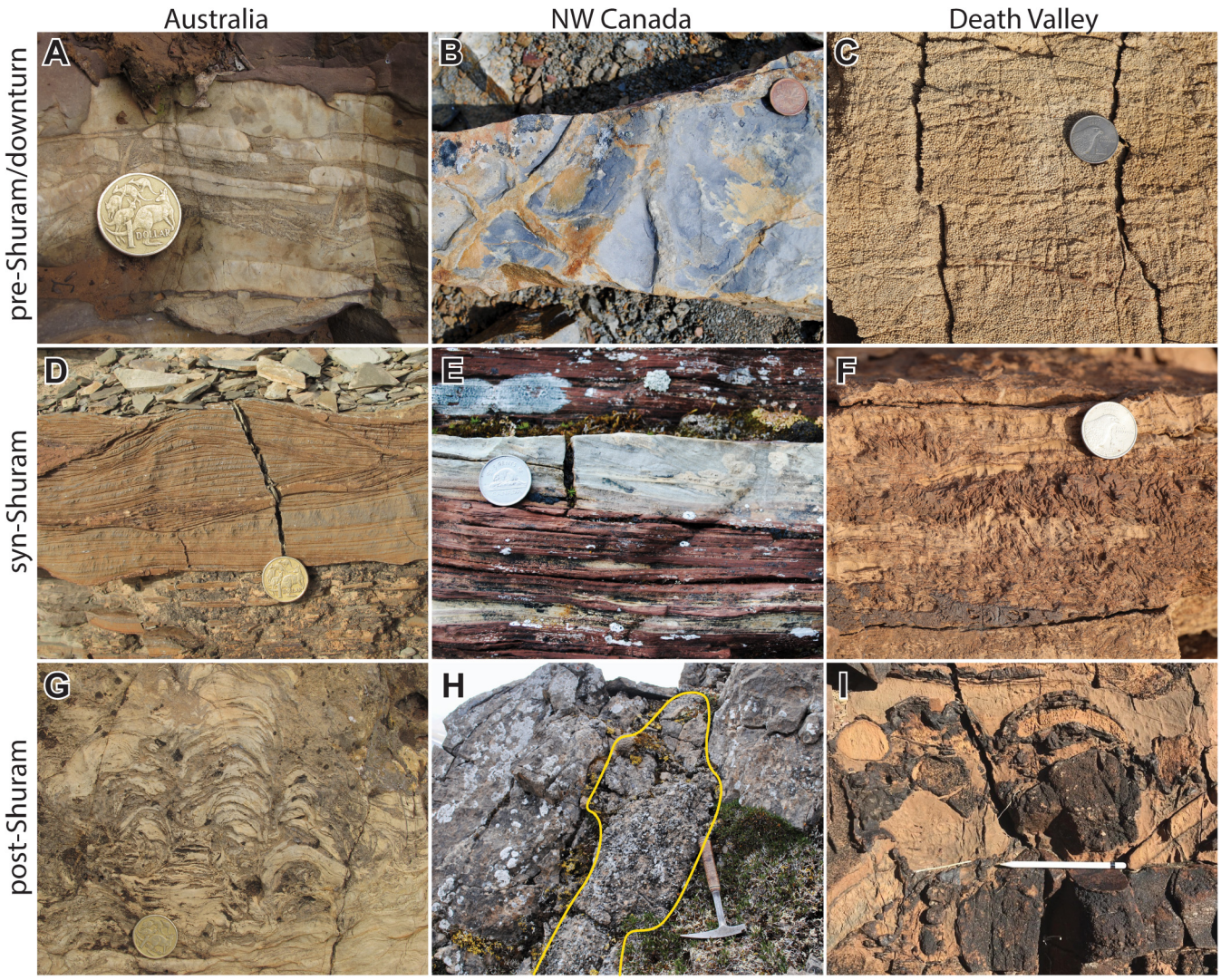

Fig. 2. Photo panel of representative lithofacies from pre-, syn-, and post-Shuram CIE intervals. (A) 0.1-1 m thick intraclast tabular rudstone of the "Wearing Dolomite" marks the base of unit 1 of the Wonoka Fm, Australia, (B) mudcracks along a bedding surface of interbedded siltstone and quartz arenite at the contact between the Nadaleen and Gametrail formations in the Goz Creek area, Northwest Canada, (C) cross-stratified oolitic dolograinstone of the "Johnnie oolite" in the Rainstorm Member of the Johnnie Fm, Death Valley, (D) cross-stratified silty limestone common throughout units 4-5 of the Wonoka Fm, Australia, (E) maroon and gray-weathering thin-bedded silty limestone with partial-Bouma sequences in the lower Gametrail Fm in the Nadaleen River area of Northwest Canada, (F) pink-weathering limestone with aragonite crystal fan pseudomorphs in the Rainstorm Member of the Johnnie Fm, Death Valley, (G) stromatolitic doloboundstone comprising bioherms in unit 11 of the Wonoka Fm, Australia, (H) karst cavity (outlined in yellow) of granule- to cobble-sized clasts of carbonate, chert, and quartzite in a carbonate-cemented quartz sand matrix in contact with vuggy, recrystallized dolostone of the upper Gametrail Fm in the Goz Creek area of Northwest Canada, (I) carbonate-clast breccia comprising "paleocanyon fill" at the contact between the Johnnie and Stirling formations in Death Valley. (For interpretation of the colors in the figure(s), the reader is referred to the web version of this article.)

maximum flooding interval) occurs roughly halfway between the base and top of the syn-Shuram interval (Fig. 3). This maximum flooding interval also marks a shift from the distinctly maroon-colored beds of unit 3 in Australia (Fig. 2A), the lower Gametrail Fm in distal locations of Northwest Canada (Fig. 2B, 3), and the lower Shuram Fm in Oman. In contrast, post-Shuram strata in all studied locations mark a return to shallower-water carbonate and siliciclastic sedimentation across a prominent regressive sequence boundary (Fig. 3).

4.2. Geochemical expression of the Shuram CIE

4.2.1. Stratigraphic trends

Pre-Shuram strata, where carbonate, are marked by positive $\delta^{13}C$ values up to +10‰, relatively positive $\delta^{44/40}Ca$ values ranging from −1.2 to −0.3‰, and high Mn/Sr and low Sr/Ca ratios (Fig. 3). In contrast, the nadir of the Shuram CIE is marked by negative $\delta^{13}C$ values down to −15‰, $\delta^{44/40}Ca$ values ranging from −1.8 to −1‰, and high Mn/Sr and low Sr/Ca ratios (Fig. 3). The syn-Shuram strata, roughly halfway between the nadir and termination of the excursion, contain an interval of consistent $\delta^{13}C$ values (∼−8 to −6‰), generally the most negative $\delta^{44/40}Ca$ values of the Shuram CIE (down to −2‰), low Mn/Sr ratios, and the highest Sr/Ca ratios of the excursion (shaded interval of Fig. 3). The transition to post-Shuram strata is accompanied by a return in $\delta^{13}C$ to ≥0‰, $\delta^{44/40}Ca$ of ∼−1‰, and high Mn/Ca and low Sr/Ca ratios (Fig. 3).

As highlighted above, the interval that contains the most negative $\delta^{13}C$ values of the Shuram CIE nadir does not coincide with most negative $\delta^{44/40}Ca$ values in most locations (Fig. 3). The most depleted $\delta^{13}C$ values occur at the base of the Shuram, while peak negative $\delta^{44/40}Ca$ values occur just above this interval, roughly halfway between the nadir and recovery to 0‰ in strata with a $\delta^{13}C$ range of ∼−8 to −6‰ (shaded interval of Fig. 3). This interval of low $\delta^{44/40}Ca$ occurs within the maximum flooding interval

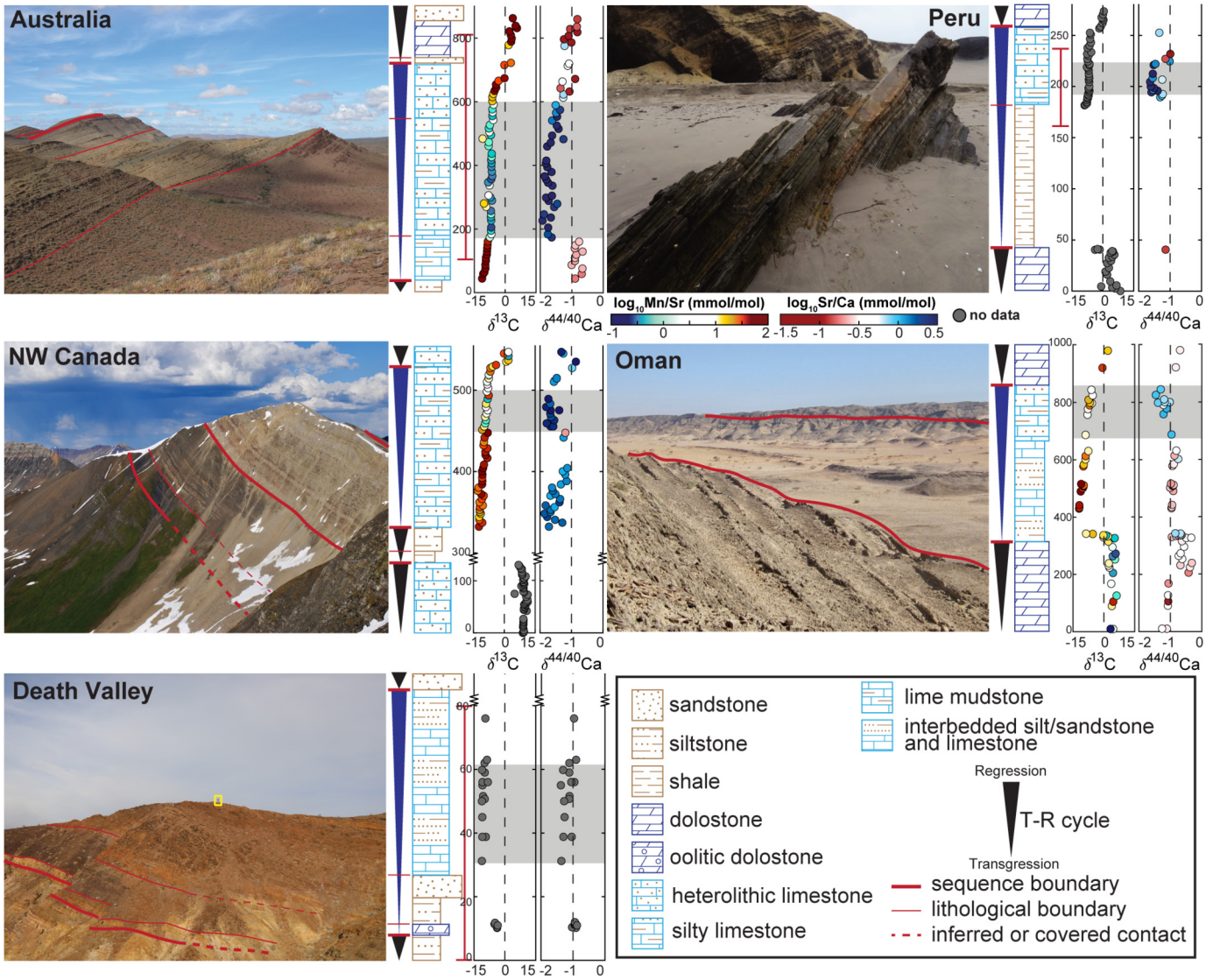

Fig. 3. Representative field photographs and generalized stratigraphic data for the Shuram CIE localities. Red bars next to the stratigraphic plots indicate the observable strata in the photograph. All locations record a significant transgression at the base of the Shuram CIE and a progressive shoaling towards a sequence boundary at the return to 0‰ in $\delta^{13}C$ (represented by the blue-colored T-R cycle). The onset of this transgression marks a sharp change in the lithofacies, with a shift from either shallower siliciclastic or dolostone facies to deeper-water limestone at the sequence boundary. The carbonate at the base of the Shuram transgression generally contain the most negative $\delta^{13}C$, higher Mn/Sr, and less negative $\delta^{44/40}Ca$ when compared with the maximum flooding interval that coincides with maximum Sr/Ca, lower Mn/Sr, and minimum $\delta^{44/40}Ca$ values in each of these profiles (shaded in gray). Note that the vertical scale for the Northwest Canada and Death Valley stratigraphic plots is truncated to better display the key intervals. The Peru panel shows the lowermost carbonate interbedded with siltstone of unit SJ2 in the foreground, while the contact between carbonate-dominated and black-shale dominated intervals is visible in the background. Geoscientist for scale outlined in yellow in the Death Valley panel.

at most locations and is associated with the highest observed Sr/Ca values and lower Mn/Sr ratios (Fig. 3), although in NW Canada there are similarly negative $\delta^{44/40}Ca$ values throughout the CIE until its termination (Fig. 3).

4.2.2. Water depth trends

A prominent water-depth gradient exists for multiple geochemical proxies in the Shuram CIE dataset (Fig. 4, 5). In general, the samples from deeper-water slope and outer-shelf depositional environments are predominantly limestone and bear the most negative $\delta^{44/40}Ca$ and $\delta^{13}C$ values (~ -15 to -8‰) and have higher Sr/Ca and U/Ca ratios (Fig. 4, 5). In contrast, samples from inner and middle ramp environments have more positive $\delta^{44/40}Ca$ (~ -1.4 to -0.3‰) and $\delta^{13}C$ (~ -6 to $+8$‰) values; these samples also have lower Sr/Ca and U/Ca ratios and are predominantly dolostone. Although dolostone samples with coupled $\delta^{26}Mg$ and $\delta^{44/40}Ca$ data are limited ($n = 111$), middle ramp dolostones tend to have more negative $\delta^{44/40}Ca$ and positive $\delta^{26}Mg$ values while inner ramp dolostones tend to have negative $\delta^{26}Mg$ and positive $\delta^{44/40}Ca$ values (Fig. 4C). On average, limestone samples have lower Mn/Sr and more negative $\delta^{44/40}Ca$, while dolostone and shallow-water limestone samples have higher Mn/Sr and are more positive in $\delta^{44/40}Ca$ (Fig. 4D), similar to trends from the modern Bahamas Banks (Fig. 4E).

Binning the geochemical data by water depth further demonstrates that deeper-water environments have more negative $\delta^{44/40}Ca$ and $\delta^{13}C$ values compared to shallower-water environments throughout the excursion (Fig. 6). In the Shuram nadir and recovery, deeper-water $\delta^{13}C$ values are also more negative than their shallow-water equivalents (Fig. 6). This is especially apparent in Northwest Canada, where inner ramp dolostones reach a $\delta^{13}C$ nadir of ~ -6‰, while slope limestones are close to -15‰ (Fig. 6). Pre- and post-Shuram intervals characterized by more positive $\delta^{13}C$ values show no apparent water depth gradient (Fig. 6).

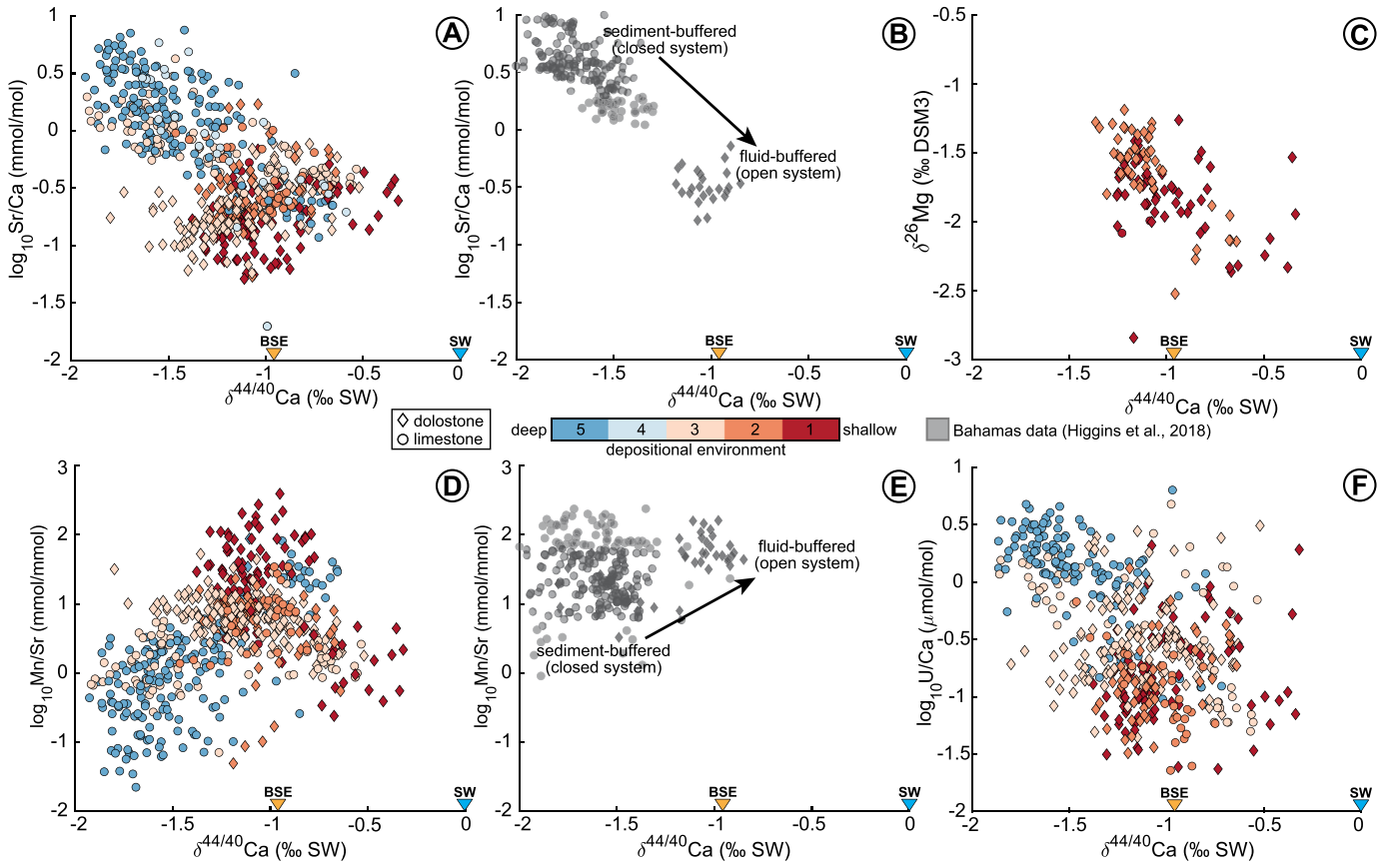

Fig. 4. Cross-plots of geochemical data from the Shuram CIE and the Bahamas Bank (gray data; Higgins et al., 2018). Sample symbology indicates bulk mineralogy (limestone vs. dolostone) and color represents relative water depth by depositional environment. (A) $\log_{10}$Sr/Ca vs. $\delta^{44/40}$Ca, (B) $\log_{10}$Sr/Ca vs. $\delta^{44/40}$Ca for Bahamas data, (C) δ^{26}Mg vs. $\delta^{44/40}$Ca, (D) $\log_{10}$Mn/Sr vs. $\delta^{44/40}$Ca, (E) $\log_{10}$Mn/Sr vs. $\delta^{44/40}$Ca for Bahamas data, (F) U/Ca vs. $\delta^{44/40}$Ca. BSE = bulk silicate Earth (−0.96‰; Skulan et al., 1997); SW = seawater (0‰). Depositional environment color coding is as follows: 1 = inner ramp, 2 = middle ramp, 3 = mid-outer ramp, 4 = outer ramp, 5 = slope.

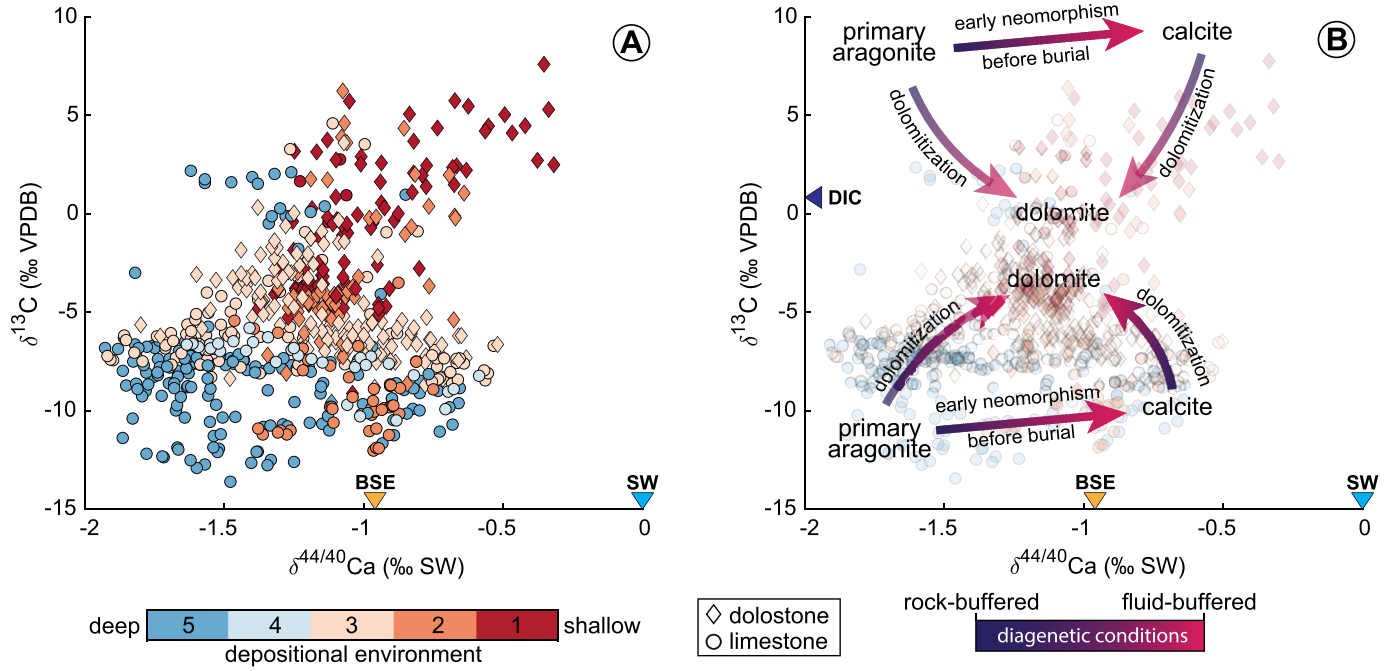

Fig. 5. Cross-plot of (A) δ^{13}C vs. $\delta^{44/40}$Ca data and (B) annotation of the same cross-plot. Arrows in panel (B) are colored to represent the prevailing diagenetic conditions between rock- and fluid-buffered end-members during dolomitization of primary aragonite or early neomorphism from primary aragonite to calcite. DIC = dissolved inorganic carbon of modern seawater (~0.8‰; Kroopnick, 1985). Depositional environment color coding is as follows: 1 = inner ramp, 2 = middle ramp, 3 = mid-outer ramp, 4 = outer ramp, 5 = slope.

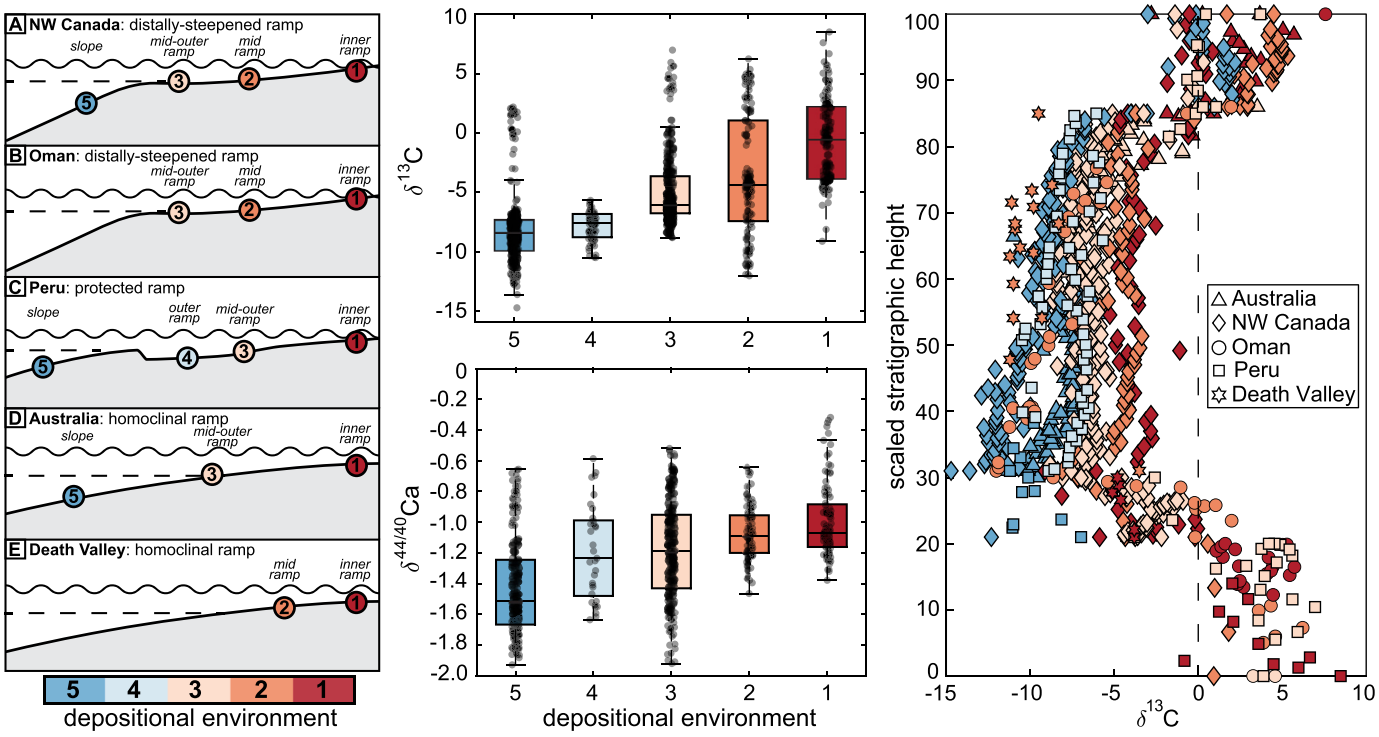

Fig. 6. Schematic representation of carbonate platform morphologies and depositional environments represented at the Shuram CIE localities. Dashed lines represent approximate water depth of maximum storm wave base. $\delta^{13}C$ and $\delta^{44/40}Ca$ gradients occur with water depth, where increasing water depth is associated with more negative $\delta^{44/40}Ca$ and $\delta^{13}C$. All $\delta^{13}C$ means are statistically significant from one another ($p < 0.01$) except for the slope and outer ramp. The slope $\delta^{44/40}Ca$ mean is significantly different from all others ($p < 0.01$), and the inner ramp $\delta^{44/40}Ca$ mean is significantly different from all others except for the middle ramp ($p < 0.01$). The mid-outer and outer ramp $\delta^{44/40}Ca$ means are not significantly different from one another. Depositional environment color coding is as follows: 1 = inner ramp, 2 = middle ramp, 3 = mid-outer ramp, 4 = outer ramp, 5 = slope.

5. Discussion

5.1. Base level change during the Shuram CIE

5.1.1. Sequence stratigraphy and estimates of base level change

At each studied location, the Shuram CIE occurs in a single transgressive-regressive (T-R) sequence (Fig. 3). Although the amount of flooding associated with the onset and nadir of the Shuram CIE is difficult to quantify, it can be broadly estimated by comparison with modern and ancient marine depth gradients. For example, the Wonoka Fm contains evidence for a shift from slope sedimentation (e.g., silty turbiditic limestone with flute casts and Bouma sequences) at the base of the CIE to inner ramp deposition at its culmination (e.g., doloboundstone and cross-stratified sandstone), while sections in Oman, Peru, and Death Valley record shifts from outer to middle ramp depositional environments in the nadir to inner ramp settings at the termination of the overlying regressive sequence (Fig. 3). In addition, the post-Shuram subaerial exposure surface and associated paleokarst in Northwest Canada (Fig. 2H) provides a local minimum zero water depth constraint at the Shuram CIE's termination. Other locations not examined in this study also record a similar sequence stratigraphic trend to those described herein (e.g., Grotzinger et al., 2011), with a sequence boundary separating pre- and syn-Shuram strata observed in member 3 of the Doushantuo Fm in South China and the Nikol'skaya Fm in Siberia (e.g., Jiang et al., 2011; Melezhik et al., 2009).

Based on the coordinated shifts in depositional environments through the Shuram T-R sequence on these different paleocontinents, we estimate relative sea level change on the order of 10s of meters, if not perhaps 100s of meters (see below); thus, if truly coincident this most likely reflects a eustatic signal. Importantly, there is some variability in the observed shifts in depositional environments, sedimentary facies, and stratigraphic thicknesses between each Shuram-bearing locality, where some sites may have accommodated >500 m of base level change (e.g., Wonoka Fm) while others could record less than 50 m (e.g., Doushantuo Fm, South China). This variability requires that the interpreted eustatic signal be superimposed on regional basin subsidence histories.

5.1.2. Potential drivers of base level change

The Shuram transgression is consistent in magnitude with continental ice sheet contraction and expansion (<~200 m, rate of 20 m per thousand years (ky)), ocean basin volumetric adjustment from changes in seafloor spreading rates or ocean ridge lengths (~100-300 m, 10 m/My), and/or the emplacement of oceanic plateaus (~0-60 m, variable rates) (Miller et al., 2005). The transgression's magnitude and variability are also consistent with base level changes due to local or regional tectonic subsidence, which can be driven by flexure, thermal, or mechanical processes (Watts, 1982). As highlighted above, the large degree of variation in the magnitude of base-level change between individual Shuram-bearing locations suggests that tectonic subsidence likely played some role in the local expression of the transgression. For example, there is evidence that salt diapirism may have influenced Neoproterozoic basin evolution in Australia (Rowan et al., 2020), and there is also evidence for active tectonism in Peru during the Shuram CIE (Hodgin, 2020). However, given the consistent age constraints on the Shuram CIE (Rooney et al., 2020), these local tectonic subsidence histories likely do not explain what appears to be a globally synchronous transgression.

Widespread magmatism and plate reorganization can affect changes in mid-ocean ridge and orogen length, both of which can drive eustatic changes (e.g., Miller et al., 2005). Widespread Ediacaran magmatism concurrent with the Shuram CIE is recorded by the Central Iapetus magmatic province (e.g., Youbi et al., 2020,

and references therein) and ca. 577-553 Ma rifting of the Iapetus margin of Laurentia (e.g., Aleinikoff et al., 1995; Tanczyk et al., 1987; van Staal et al., 2013). Similar age Ediacaran rifting and localized magmatism also occurred on the Cordilleran margin of Laurentia (e.g., Colpron et al., 2002). These rift-related events also broadly coincide with the West Gondwana orogeny (e.g., Caxito et al., 2021). Significant increases in mid-ocean ridge and orogen lengths during middle-late Ediacaran plate reorganizations could provide a viable mechanism that satisfies both the magnitude of the Shuram transgression and current estimates for the ca. 6-7 My duration of the CIE (Rooney et al., 2020). Similar plate-scale tectonic processes have also been invoked for global transgressions which occurred during the reorganization of the Pacific (ca. 100 Ma) and Atlantic (ca. 200-190 Ma) oceans (Heller and Angevine, 1985; Kominz, 1984; Müller et al., 2008).

5.2. Geochemical trends

5.2.1. Influence of diagenesis

All the geochemical proxies display variability that is strongly partitioned by water depth across the Shuram CIE (Figs. 4–6). Diagenetic studies on modern and ancient carbonate rocks using $\delta^{44/40}$Ca and δ^{26}Mg isotopes, in conjunction with geochemical modeling, have shown that the extent of carbonate diagenesis during neomorphism, dissolution and reprecipitation, or dolomitization can be characterized as being buffered with respect to the surrounding rock (sediment-buffered) or seawater (fluid-buffered) (Ahm et al., 2018; Higgins et al., 2018). Thus, the Shuram CIE trends may represent a range of diagenetic conditions between fluid- and sediment-buffered end-members (e.g., Ahm et al., 2018). Calcium isotopes, Sr/Ca, and U/Ca ratios can distinguish between these diagenetic end-members because calcium isotope fractionation and Sr and U partitioning are controlled by mineralogy and precipitation rate (DeCarlo et al., 2015; Gussone et al., 2005). In particular, primary aragonite and calcite are more depleted in ^{44}Ca (i.e., more negative $\delta^{44/40}$Ca values) and enriched in Sr and U relative to diagenetic calcite and dolomite, which have lower Sr and U and more positive $\delta^{44/40}$Ca values that approach pore fluid compositions, with fractionations of ∼0‰ at equilibrium (Fantle and DePaolo, 2007).

The shallow-water limestone and dolostone deposited during the pre- and post-Shuram CIE intervals with more positive $\delta^{44/40}$Ca, and low Sr/Ca and U/Ca ratios likely experienced more fluid-buffered diagenesis during dolomitization of an aragonite precursor and have δ^{13}C compositions strongly influenced by the altering fluid(s) (Fig. 4, 5). Specifically, their more positive δ^{13}C and $\delta^{44/40}$Ca values could reflect alteration towards seawater values which today are ∼0‰ in $\delta^{44/40}$Ca and ∼0‰ in δ^{13}C (Fig. 5). In contrast, the deeper-water limestone deposited during the Shuram transgression, which are characterized by more negative $\delta^{44/40}$Ca and high Sr/Ca and U/Ca ratios, likely experienced sediment-buffered diagenesis during neomorphism from aragonite to calcite, as the Sr/Ca and U/Ca values approach aragonite compositions from modern shallow marine sediment, coral skeletons, and laboratory experiments (Figs. 3-5; Ahm et al., 2018; Banner, 1995; DeCarlo et al., 2015; Higgins et al., 2018). As such, the geochemistry of these sediment-buffered rocks would remain close to their primary composition with respect to diagenesis-resistant proxies like δ^{13}C. The differences in Sr/Ca and $\delta^{44/40}$Ca between fluid-buffered shallow dolostones and sediment-buffered slope limestones are also consistent with data from the modern Bahamas Banks that show similar trends between platform dolostones and slope limestones (Fig. 4B; Higgins et al., 2018).

5.2.2. Reworking of platform carbonate during initial flooding

Some of the most negative δ^{13}C values that comprise the Shuram nadir at the base of the T-R sequence have more positive $\delta^{44/40}$Ca values (ranging ∼ −0.6‰ to −1.5‰), which could suggest they are fluid-buffered despite being deposited in a deep-water setting (Fig. 3, 5; Ahm et al., 2018). However, a simple fluid-buffered interpretation for these deeper-water limestones with more positive $\delta^{44/40}$Ca is difficult to reconcile with their interpretation as slope and outer ramp carbonates deposited at the base of a transgression without any clear field or petrographic evidence for significant fluid flow (Fig. 3). These data can instead be explained through reworking of platform carbonate that underwent early fluid-buffered neomorphism from aragonite to calcite in the same ^{13}C-depleted fluid from which it precipitated, prior to transport to the slope (Fig. 5, 7). Once transported from the platform to the slope, the fluid-buffered calcite would likely preserve these early diagenetic values with more positive $\delta^{44/40}$Ca (∼−0.5‰) and depleted δ^{13}C values (∼−11‰).

Alternatively, if these carbonates originally were primary calcite, which is ∼0.5‰ more positive in $\delta^{44/40}$Ca and has lower Sr and U than primary aragonite precipitating from the same fluid (Gussone et al., 2005), then this stratigraphic interval could be interpreted as being sediment-buffered (Husson et al., 2015a). In this scenario, the shifts in $\delta^{44/40}$Ca between the nadir and syn-Shuram intervals could represent a shift in primary mineralogy from calcite to aragonite, rather than a shift from fluid- to sediment-buffered diagenetic conditions (Fig. 3; Husson et al., 2015a). Bergmann et al. (2018) suggested that the Nafun Group of the Huqf desert, including the Khufai, Shuram, and Buah formations, did not experience fluid-buffered diagenesis or peak temperatures able to drive solid state reordering, consistent with the more positive $\delta^{44/40}$Ca values from the nadir interval in Oman reflecting a primary calcite mineralogy. However, samples from NW Canada have consistently negative $\delta^{44/40}$Ca values (∼−1.7‰) throughout the CIE (Fig. 3, 7) and thus lack evidence for a shift in primary mineralogy between the beginning and end of the excursion.

5.3. Calcium and carbon isotope mass balance

Interpretations of C and Ca isotopes that invoke changes to the global marine reservoirs of these major elements must consider both local effects and global isotopic mass balance (i.e., inputs = outputs at steady state). Here, we emphasize these requirements for interpreting C and Ca isotope systems in the context of preserving mass balance, while also highlighting the potential for non-steady state behavior within local systems not representative of global reservoirs.

5.3.1. Requirements for a global perturbation to Ca and C oceanic reservoirs

The global Ca cycle is comprised of inputs from riverine and hydrothermal sources ($\delta^{44/40}$Ca = ∼−0.96‰ equal to bulk silicate Earth, BSE) that are balanced by a single sink – calcium carbonate burial (Fantle and Tipper, 2014). Any point-by-point synchronous interpretation of marine $\delta^{44/40}$Ca data therefore requires that average carbonate outputs be equal to BSE on timescales longer than the residence time of Ca in the oceans (ca. 1 My; Blättler and Higgins, 2017; Sarmiento and Gruber, 2006). If the measured $\delta^{44/40}$Ca values are assumed to represent average carbonate output and are measured from correlative strata, it becomes difficult to reconcile the observed large changes in $\delta^{44/40}$Ca during the Shuram CIE with the requirement of Ca isotope mass balance given that it apparently occurred over >1 My (ca. 6-7 My; Rooney et al., 2020). Because the Ca isotope system responds quickly to changes in input/output fluxes due to the dependence of both calcium carbonate precipitation and dissolution on the carbonate saturation

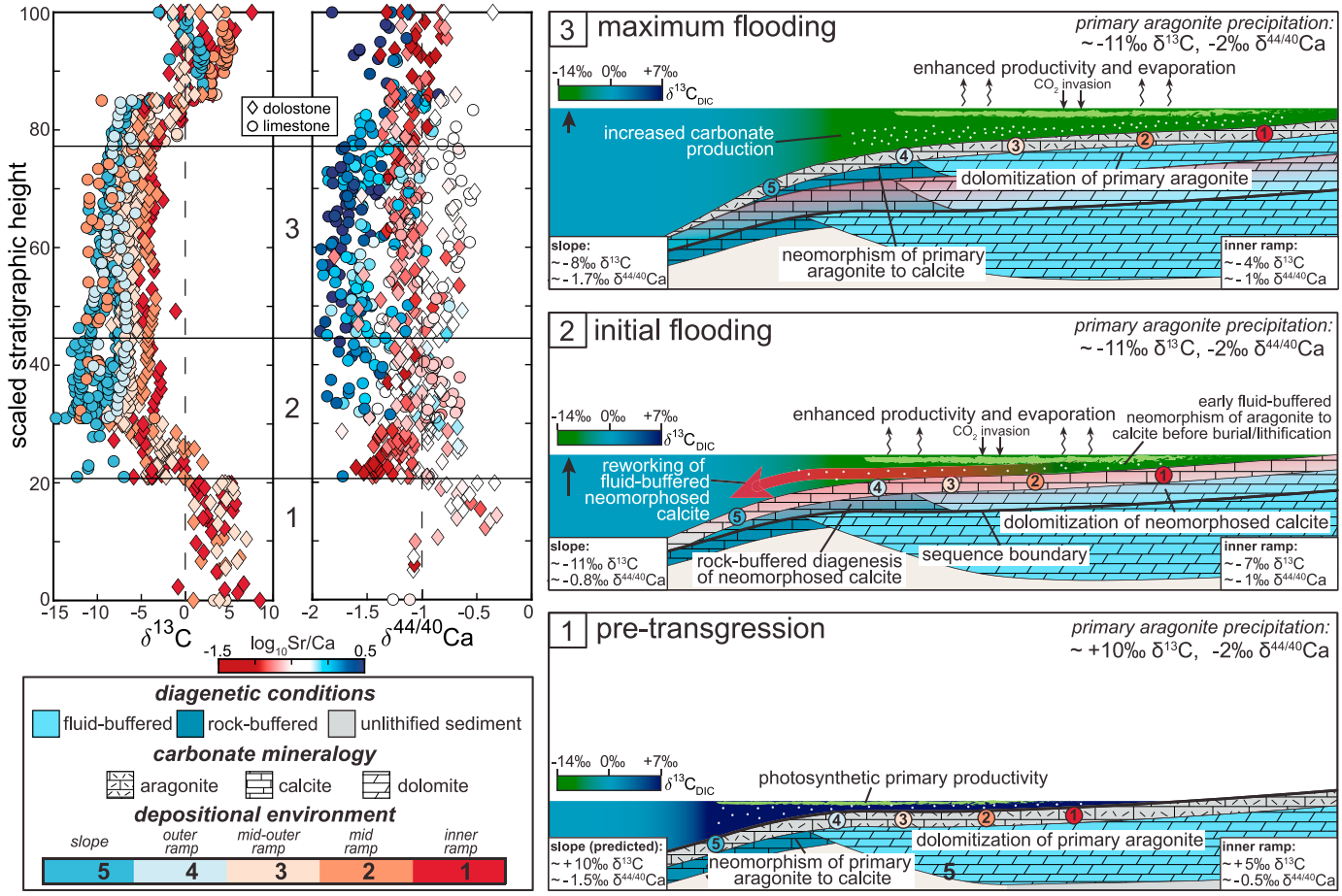

Fig. 7. Hypothesized link between base level change and drivers for $\delta^{13}C$ and $\delta^{44/40}Ca$ changes across the Shuram CIE. (1) Pre-Shuram CIE interval characterized by sea level lowstand where carbonate ramps are subject to pervasive dolomitization and/or subaerial exposure and locally positive $\delta^{13}C_{DIC}$ is maintained by diurnal cycling of organic matter from photosynthetic primary productivity (Geyman and Maloof, 2019). No samples in this dataset from the pre-Shuram interval are from the slope, but they are predicted to undergo sediment-buffered diagenesis and preserve more positive $\delta^{13}C$ values compared with the inner ramp. (2) Initiation of flooding expands the area of shallow depositional environments where enhanced productivity and evaporation drives CO_2 invasion and isotope reservoir effects push $\delta^{13}C_{DIC}$ to negative values of the CIE nadir. Reworking of primary aragonite sediment in shallower-environments drives early fluid-buffered neomorphism to calcite during transport to the slope (red-colored sediment). (3) Transgression reaches interval of maximum flooding possibly coincident with increased carbonate production and rapid precipitation, driving trace metal enrichments and negative $\delta^{44/40}Ca$ values down to ~−2‰. Continued primary productivity and coupled isotope reservoir effects maintain local $\delta^{13}C_{DIC}$ at highly negative values.

state (Komar and Zeebe, 2016), even on sub-My timescales there should be an approximate balance between the Ca isotopic composition of weathering sources (BSE, ~−0.96‰; Blättler and Higgins, 2017; Skulan et al., 1997) and carbonate sinks.

The canonical carbon cycle steady state model is that volcanic inputs of CO_2 (~−5‰) are balanced by two sinks, calcium carbonate precipitation ($\delta^{13}C$ = ~+1‰) and organic C burial ($\delta^{13}C$ = ~−29‰) (e.g., Kump and Arthur, 1999). A $\delta^{13}C$ excursion of the magnitude observed (up to ~25‰) occurring over an estimated duration of ca. 6-7 My (Rooney et al., 2020) is difficult to reconcile in terms of C isotope mass balance in this simple model. Injections of isotopically negative C (e.g., from methane release) drive transient negative excursions of varying magnitudes that generally last less than 1 My (e.g., Kump and Arthur, 1999). This model for $\delta^{13}C$ excursions underscores the difficulty of maintaining a global DIC reservoir with values less than the mantle input (~−5‰) for much longer than the residence time of C in the oceans (ca. 0.1 My).

5.3.2. Shuram CIE as a local phenomenon

One possibility for reconciling Ca and C isotope mass balance with the large changes observed in $\delta^{44/40}Ca$ and $\delta^{13}C$ data from the Shuram CIE is that the disparate continental margins examined herein were disconnected from average global marine DIC during the excursion (Fig. 7). This is also possible if the successions with the Shuram CIEs are not precisely synchronous in timing or duration, even though they occur within the same ~6-7 My window of geologic time. Indeed, many of the localities with the Shuram CIE remain undated (Rooney et al., 2020). Alternatively, the Shuram-bearing strata could be synchronous but not reflective of the average $\delta^{44/40}Ca$ values of buried carbonate minerals. In this case, another carbonate sink enriched in ^{44}Ca and ^{13}C must exist to compensate for the low $\delta^{44/40}Ca$ and $\delta^{13}C$ values generally associated with the CIE. One possibility is that, in addition to strata recording the Shuram CIE, there are also coeval carbonate sediments that have undergone fluid-buffered alteration by seawater and do not contain the characteristic negative $\delta^{13}C$ values (similar to what has been discussed for the Trezona CIE; Ahm et al., 2021). The observed depth dependence of $\delta^{44/40}Ca$ and $\delta^{13}C$ (Fig. 4–6) supports this scenario, where the more fluid-buffered successions contain smaller CIEs. Other possibilities for sinks with more positive $\delta^{44/40}Ca$ include authigenic carbonate (Blättler et al., 2015) and carbonate veins in oceanic crust, which generally have $\delta^{44/40}Ca$ values higher than BSE (Blättler and Higgins, 2017).

5.4. Potential drivers of the Shuram CIE

Recent studies have highlighted how Neoproterozoic sea level fluctuations may have influenced the expression of various CIEs through altering the diagenetic conditions experienced by shallow water carbonate rocks (Ahm et al., 2021; Bold et al., 2020; Hoffman and Lamothe, 2019). We now explore several proposed drivers for the Shuram CIE that are linked with eustatic fluctuations and reconcile them with the new geochemical data presented herein. We emphasize that these explanations need not be, and likely are not, mutually exclusive.

5.4.1. Diagenesis and authigenesis

Numerous studies have proposed that the Shuram CIE may not be representative of global seawater DIC and instead represents post-depositional alteration during meteoric (Knauth and Kennedy, 2009) or burial diagenesis (Derry, 2010). Other studies have proposed the excursion is caused by widespread early marine diagenesis associated with the precipitation of authigenic carbonate that became incorporated into Shuram CIE successions (Laakso and Schrag, 2020; Macdonald et al., 2013; Schrag et al., 2013).

Meteoric diagenesis as a driver for the excursion is inconsistent with the sedimentological, geochemical, and stratigraphic data presented herein that indicate the base of the excursion is associated with significant flooding of all examined carbonate margins (Fig. 3). Most of the deep-water limestones deposited at the base of the transgression, which have the most negative $\delta^{13}C$ values, are also interpreted here to be sediment-buffered after deposition (Fig. 5), which is the opposite of what would be expected if meteoric diagenesis was indeed the driver for the Shuram CIE. Although there is evidence for subaerial exposure and fluid-buffered diagenesis at the upper sequence boundary of the Shuram T-R sequence (Fig. 2H, 3), the available geochemical data indicate that meteoric fluids did not infiltrate deep enough to influence the syn-Shuram rocks deposited at the base of the transgression, nor did they alter the local host dolostones to the extent that they no longer bear the negative $\delta^{13}C$ values of the CIE (Fig. 4, 5).

Burial diagenesis as a driver for the Shuram CIE is inconsistent with isotope conglomerate tests performed on the Wonoka Formation in Australia (Husson et al., 2015b) and with the geochemical data presented herein (low $\delta^{44/40}Ca$ values and high Sr/Ca ratios, Fig. 4). The isotope conglomerate tests indicate that very negative bulk $\delta^{13}C$ and $\delta^{18}O$ values were acquired in Wonoka carbonates before erosion and re-deposition into penecontemporaneous breccia deposits present at some localities and could not have been developed as a result of late-stage burial diagenesis (Husson et al., 2012). Burial diagenesis is also not consistent with the regional N-S isotopic pattern that follows the transgression preserved in the Johnnie Fm of Death Valley (Bergmann et al., 2011).

Classically employed sampling protocols may actively bias against textures indicative of authigenic carbonate, but extensive petrographic examination of the samples included in this compilation identified no significant authigenic phases approaching the proposed ~45% portion of all precipitated carbonate required to drive the Shuram CIE (Laakso and Schrag, 2020). We also did not identify any positive $\delta^{13}C$ outlier values from within the Shuram CIE. Although SIMS analyses of samples from the Shuram nadir in Australia found an authigenic dolomite phase with more positive $\delta^{13}C$ values (~ -5 to $+6‰$), point counts of these same samples suggested these phases were an insignificant component of the bulk carbonate (between 3% and 20%; Husson et al., 2020). In addition, the carbonate samples measured here with the most negative $\delta^{13}C$ values comprise outer shelf and slope deposits dominated by suspension deposition of detrital carbonate, with no evidence for void-filling or porosity-occluding cements, seafloor precipitates, or secondary nodules which would potentially comprise the hypothesized deep-water authigenic carbonate sink (Fig. 2D-F).

There is no obvious prediction for authigenic carbonate production as it relates to base level fluctuations, but condensed sedimentary horizons, which often concentrate phosphatic, ferromanganese, and carbonate authigenic minerals, commonly occur at the base of the transgressive sequences or at the interval of maximum flooding (e.g., Föllmi, 2016). This would suggest that the rocks at the base of the Shuram excursion flooding sequence would be subject to the largest amount of condensation; however, these strata notably lack characteristic authigenic textures common in condensed horizons. This could indicate that carbonate production and accumulation rates were sufficiently high during the Shuram transgression to preclude significant condensation and authigenesis.

5.4.2. Linked global transgression and local changes to DIC

Global marine transgressions can influence the distribution of shallow carbonate environments in profound ways. In the case of shallow-gradient carbonate ramps, which fit the platform architecture for most locations considered herein (Fig. 6), it is expected that a large transgression would have significantly expanded carbonate inner to middle ramp sedimentation. Shallow-water marine environments are generally conducive to enhanced evaporation and associated carbonate precipitation, and during periods of marine evaporation (and photosynthetic primary productivity), isotope reservoir effects in partially restricted water masses can drive local DIC to extreme depleted (Lazar and Erez, 1990) or enriched (Stiller et al., 1985) compositions. Photosynthetic drawdown in these restricted water mass systems may drive atmospheric CO_2 invasion, leading to large fractionations in $\delta^{13}C_{DIC}$ (up to $-14‰$) (Lazar and Erez, 1990), although this process is associated with notable declines in carbonate saturation state.

We suggest that a global transgression paired with enhanced evaporation and shallow-water primary productivity may have created an ideal scenario in which newly flooded carbonate ramps and platforms were disconnected from open marine DIC and subject to carbonate isotopic reservoir effects (Fig. 7). This scenario would be capable of driving local ramp or platformal DIC to extremely depleted values that could be captured in rapidly accumulating shallow-water carbonates (and redeposited deeper-water sediments) without requiring unrealistic changes to the global carbon cycle. Temporary oceanographic disconnection of shallow water masses from the global oceans is consistent with the observed aged water masses and variable carbonate isotopic compositions observed on the modern Bahama Bank (Geyman and Maloof, 2019, and references therein). In addition, high rates of Ediacaran primary productivity (e.g., Gao et al., 2020), which could be reflected in the highly positive $\delta^{13}C$ background state of Ediacaran carbonates (e.g., Ahm et al., 2021; Halverson et al., 2010; Kaufman et al., 1997), may have provided the local reductants to facilitate this type of scenario without the need to invoke intense evaporative conditions such as those seen in modern CO_2 invasion scenarios (e.g., Lazar and Erez, 1990). In fact, there are no recorded evaporites in the Shuram-bearing strata examined herein (see Cui et al. (2021) for a recent compilation of sulfate minerals through the Shuram CIE), and there is no reason to believe that local ramp or platformal restriction and evaporation was significant enough to initiate the precipitation of evaporites beyond carbonate minerals.

This scenario has specific predictions for the fractionation imparted on carbon by photosynthesis in shallow-water Ediacaran environments. If local pre-excursion positive $\delta^{13}C_{DIC}$ was maintained through diurnal cycling of organic matter (Geyman and Maloof, 2019), such that primary producers were not CO_2-limited, there would likely have been a larger fractionation between DIC and organic carbon (Popp et al., 1998). In contrast, the drawdown

of surface water DIC during the CIE by intense photosynthesis would result in a smaller fractionation due to the lower concentration of CO_2 (Popp et al., 1998). $\delta^{13}C_{org}$ data from Oman and South China support this scenario, with reported decreases in $\Delta^{13}C$ of $\sim$15‰ associated with the downturn and nadir of the Shuram CIE (Lee et al., 2013; McFadden et al., 2008).

Elevated ramp or platformal evaporative conditions in shallow water settings during the Shuram CIE could have resulted in the widespread nucleation of carbonate (and elevated precipitation rates); this, in turn, may have facilitated disequilibrium between these shallow water masses and marine DIC through the associated rapid accumulation rates (Fig. 7, panel 3). The predominance of fine-grained carbonate mud in Shuram-bearing siliciclastic-dominated successions could reflect the onset of these types of nucleation-dominated conditions (e.g., Strauss and Tosca, 2020). Indeed, the rapid precipitation of carbonate during the Shuram CIE could be manifest in the $\delta^{44/40}Ca$ and trace elemental data presented herein, which are also precipitation rate dependent: higher precipitation rates commonly lead to lower $\delta^{44/40}Ca$, higher Sr/Ca, and lower Mn/Ca (Tang et al., 2008).

It is notable that other extreme Neoproterozoic CIEs are interpreted as occurring during similar order marine transgressions, such as the Bitter Springs (Halverson et al., 2007), Russøya/Islay (Halverson et al., 2018; Strauss et al., 2015), Taishir (Lau et al., 2017), and Trezona CIEs (Ahm et al., 2021). This highlights a common, yet entirely non-unique, physical forcing mechanism that may be at the core of Neoproterozoic carbonate carbon isotopic volatility. Whether the scenario described above is applicable to these CIEs or Neoproterozoic carbonate platform systems more broadly remains to be tested, as does navigating the apparent contradiction of rapid CO_2 invasion and the associated decrease in carbonate saturation states (e.g., Lazar and Erez, 1990).

6. Conclusions

We present a new compilation of stratigraphic and geochemical data from the Shuram CIE that further demonstrates the isotopic excursion is a globally synchronous primary seawater phenomenon but not representative of average global DIC. Despite occurring within a range of different depositional environments across multiple paleocontinents, our results indicate the excursion is recorded in a prominent marine flooding event and is largest in deeper-water locations where diagenesis is predominantly sediment-buffered, while the excursion is smaller in shallower-water sections with indications of more fluid-buffered diagenesis. These observations can be reconciled if the full magnitude of the CIE is largely a shallow-water phenomenon that is preferentially preserved in deep-water successions because of the better preservation potential. The evidence presented here agrees with previous studies that argue against meteoric and burial diagenesis as drivers for this excursion. We propose that carbonate margins around the world had a similar response to this global transgression but that current mass balance considerations suggest the recorded $\delta^{13}C$ and $\delta^{44/40}Ca$ isotopic values do not represent global oceanic reservoirs for these elements. Instead, the Shuram transgression may have primed shallow marine environments for enhanced productivity and/or evaporation capable of driving local isotope reservoir effects in rapidly accumulating carbonate successions.

CRediT authorship contribution statement

James F. Busch: Data curation, Investigation, Visualization, Writing – original draft. **Eben B. Hodgin:** Investigation, Writing – review & editing. **Anne-Sofie C. Ahm:** Investigation, Writing – review & editing. **Jon M. Husson:** Investigation, Writing – review & editing. **Francis A. Macdonald:** Investigation, Writing – review & editing. **Kristin D. Bergmann:** Investigation, Writing – review & editing. **John A. Higgins:** Conceptualization, Data curation, Resources, Supervision, Writing – review & editing. **Justin V. Strauss:** Conceptualization, Resources, Supervision, Writing – review & editing.

Declaration of competing interest

The authors declare that they have no known competing financial interests or personal relationships that could have appeared to influence the work reported in this paper.

Acknowledgements

We are grateful to the Tr'ondëk Hwëch'in community for granting us permission to work in the Ogilvie and Wernecke Mountains; and to Peru's Servicio Nacional de Áreas Naturales Protegidas por el Estado for granting permission to work in the Punta San Juan Reserve. KDB thanks Petroleum Development Oman for field support in Oman and Maggie Osburn for her contributions to field work in Oman. This project was supported by: National Science Foundation (NSF) grants EAR-1654131 and EAR-2021176 awarded to JVS; NSF grant EAR-1916698 awarded to FAM; Simons Foundation grant SCOL 611878 awarded to ASCA, National Geographic Society Grant EC-393R-18 awarded to JFB; a American Philosophical Society Lewis and Clark grant awarded to JFB; a Geological Society of America (GSA) graduate student research grant awarded to JFB; and field support from the Yukon Geological Survey. We thank David Moynihan, Erik Sperling, and Tom Boag for field assistance and thank Stefania Gili, Jack Murphy, and Nic Slater for assistance in the lab. We thank Boswell Wing for editorial handling of our manuscript. Finally, this contribution benefited from thoughtful reviews by Cedric Hagen and an anonymous reviewer.

Appendix A. Supplementary material

Supplementary material related to this article can be found online at https://doi.org/10.1016/j.epsl.2022.117368.

References

Ahm, A.-S.C., Bjerrum, C.J., Blättler, C.L., Swart, P.K., Higgins, J.A., 2018. Quantifying early marine diagenesis in shallow-water carbonate sediments. Geochim. Cosmochim. Acta 236, 140–159. https://doi.org/10.1016/j.gca.2018.02.042.

Ahm, A.-S.C., Bjerrum, C.J., Hoffman, P.F., Macdonald, F.A., Maloof, A.C., Rose, C.V., Strauss, J.V., Higgins, J.A., 2021. The Ca and Mg isotope record of the Cryogenian Trezona carbon isotope excursion. Earth Planet. Sci. Lett. 568, 117002. https://doi.org/10.1016/j.epsl.2021.117002.

Ahm, A.-S.C., Maloof, A.C., Macdonald, F.A., Hoffman, P.F., Bjerrum, C.J., Bold, U., Rose, C.V., Strauss, J.V., Higgins, J.A., 2019. An early diagenetic deglacial origin for basal Ediacaran "cap dolostones". Earth Planet. Sci. Lett. 506, 292–307. https://doi.org/10.1016/j.epsl.2018.10.046.

Aleinikoff, J.N., Zartman, R.E., Walter, M., Rankin, D.W., Lyttle, P.T., Burton, W.C., 1995. U-Pb ages of metarhyolites of the Catoctin and Mount Rogers formations, Central and Southern Appalachians; evidence for two pulses of lapetan rifting. Am. J. Sci. 295, 428–454. https://doi.org/10.2475/ajs.295.4.428.

Banner, J.L., 1995. Application of the trace element and isotope geochemistry of strontium to studies of carbonate diagenesis. Sedimentology 42, 805–824. https://doi.org/10.1111/j.1365-3091.1995.tb00410.x.

Bergmann, K.D., 2013. Constraints on the Carbon Cycle and Climate During the Early Evolution of Animals (Ph.D. thesis). California Institute of Technology.

Bergmann, K.D., Al Balushi, S.A.K., Mackey, T.J., Grotzinger, J.P., Eiler, J.M., 2018. A 600-million-year carbonate clumped-isotope record from the Sultanate of Oman. J. Sediment. Res. 88, 960–979. https://doi.org/10.2110/jsr.2018.51.

Bergmann, K.D., Zentmyer, R.A., Fischer, W.W., 2011. The stratigraphic expression of a large negative carbon isotope excursion from the Ediacaran Johnnie Formation, Death Valley. Precambrian Res. 188, 45–56. https://doi.org/10.1016/j.precamres.2011.03.014.

Bjerrum, C.J., Canfield, D.E., 2011. Towards a quantitative understanding of the late Neoproterozoic carbon cycle. Proc. Natl. Acad. Sci. 108, 5542–5547. https://doi.org/10.1073/pnas.1101755108.

Blättler, C.L., Higgins, J.A., 2017. Testing Urey's carbonate–silicate cycle using the calcium isotopic composition of sedimentary carbonates. Earth Planet. Sci. Lett. 479, 241–251. https://doi.org/10.1016/j.epsl.2017.09.033.

Blättler, C.L., Miller, N.R., Higgins, J.A., 2015. Mg and Ca isotope signatures of authigenic dolomite in siliceous deep-sea sediments. Earth Planet. Sci. Lett. 419, 32–42. https://doi.org/10.1016/j.epsl.2015.03.006.

Bold, U., Ahm, A.-S.C., Schrag, D.P., Higgins, J.A., Jamsran, E., Macdonald, F.A., 2020. Effect of dolomitization on isotopic records from Neoproterozoic carbonates in southwestern Mongolia. Precambrian Res. 350, 105902. https://doi.org/10.1016/j.precamres.2020.105902.

Burns, S.J., Matter, A., 1993. Carbon isotopic record of the latest Proterozoic from Oman. Eclogae Geol. Helv. 86, 595–607.

Busch, J.F., Rooney, A.D., Meyer, E.E., Town, C.F., Moynihan, D.P., Strauss, J.V., 2021. Late Neoproterozoic – early Paleozoic basin evolution in the Coal Creek inlier of Yukon, Canada: Implications for the tectonic evolution of northwestern Laurentia. Can. J. Earth Sci. https://doi.org/10.1139/cjes-2020-0132.

Canfield, D.E., Knoll, A.H., Poulton, S.W., Narbonne, G.M., Dunning, G.R., 2020. Carbon isotopes in clastic rocks and the Neoproterozoic carbon cycle. Am. J. Sci. 320, 97–124. https://doi.org/10.2475/02.2020.01.

Caxito, F.A., Basto, C.F., de Lira Santos, L.C.M., Dantas, E.L., de Medeiros, V.C., Dias, T.G., Barrote, V., Hagemann, S., Alkmim, A.R., Lana, C., 2021. Neoproterozoic magmatic arc volcanism in the Borborema Province, NE Brazil: possible flare-ups and lulls and implications for western Gondwana assembly. Gondwana Res. 92, 1–25. https://doi.org/10.1016/j.gr.2020.11.015.

Chew, D., Kirkland, C., Schaltegger, U., Goodhue, R., 2007. Neoproterozoic glaciation in the Proto-Andes: Tectonic implications and global correlation. Geology 35, 1095–1098. https://doi.org/10.1130/G23768A.1.

Clapham, M.E., Corsetti, F.A., 2005. Deep valley incision in the terminal Neoproterozoic (Ediacaran) Johnnie Formation, eastern California, USA: Tectonically or glacially driven?. Precambrian Res. 141, 154–164. https://doi.org/10.1016/j.precamres.2005.09.002.

Colpron, M., Logan, J.M., Mortensen, J.K., 2002. U-Pb zircon age constraint for late Neoproterozoic rifting and initiation of the lower Paleozoic passive margin of western Laurentia. Can. J. Earth Sci. 39, 133–143. https://doi.org/10.1139/e01-069.

Cui, H., Kaufman, A.J., Xiao, S., Zhou, C., Zhu, M., Cao, M., Loyd, S., Crockford, P., Liu, X.-M., Goderis, S., Wang, W., Guan, C., 2021. Dynamic interplay of biogeochemical C, S and Ba cycles in response to the Shuram oxygenation event. J. Geol. Soc. https://doi.org/10.1144/jgs2021-081.

DeCarlo, T.M., Gaetani, G.A., Holcomb, M., Cohen, A.L., 2015. Experimental determination of factors controlling U/Ca of aragonite precipitated from seawater: Implications for interpreting coral skeleton. Geochim. Cosmochim. Acta 162, 151–165. https://doi.org/10.1016/j.gca.2015.04.016.

Derry, L.A., 2010. A burial diagenesis origin for the Ediacaran Shuram–Wonoka carbon isotope anomaly. Earth Planet. Sci. Lett. 294, 152–162. https://doi.org/10.1016/j.epsl.2010.03.022.

Fantle, M.S., DePaolo, D.J., 2007. Ca isotopes in carbonate sediment and pore fluid from ODP Site 807A: the Ca^{2+}(aq)–calcite equilibrium fractionation factor and calcite recrystallization rates in Pleistocene sediments. Geochim. Cosmochim. Acta 71, 2524–2546. https://doi.org/10.1016/j.gca.2007.03.006.

Fantle, M.S., Tipper, E.T., 2014. Calcium isotopes in the global biogeochemical Ca cycle: implications for development of a Ca isotope proxy. Earth-Sci. Rev. 129, 148–177. https://doi.org/10.1016/j.earscirev.2013.10.004.

Föllmi, K.B., 2016. Sedimentary condensation. Earth-Sci. Rev. 152, 143–180. https://doi.org/10.1016/j.earscirev.2015.11.016.

Gao, Y., Zhang, X., Xu, Y., Fang, C., Gong, Y., Shen, Y., 2020. High primary productivity during the Ediacaran Period revealed by the covariation of paired C-isotopic records from South China. In: The Precambrian-Cambrian Phosphogenic Event. Precambrian Res. 349, 105411. https://doi.org/10.1016/j.precamres.2019.105411.

Geyman, E.C., Maloof, A.C., 2019. A diurnal carbon engine explains ^{13}C-enriched carbonates without increasing the global production of oxygen. Proc. Natl. Acad. Sci. 116, 24433–24439. https://doi.org/10.1073/pnas.1908783116.

Grotzinger, J.P., Fike, D.A., Fischer, W.W., 2011. Enigmatic origin of the largest-known carbon isotope excursion in Earth's history. Nat. Geosci. 4, 285–292. https://doi.org/10.1038/ngeo1138.

Gussone, N., Böhm, F., Eisenhauer, A., Dietzel, M., Heuser, A., Teichert, B.M.A., Reitner, J., Wörheide, G., Dullo, W.-C., 2005. Calcium isotope fractionation in calcite and aragonite. Geochim. Cosmochim. Acta 69, 4485–4494. https://doi.org/10.1016/j.gca.2005.06.003.

Halverson, G.P., Kunzmann, M., Strauss, J.V., Maloof, A.C., 2018. The Tonian-Cryogenian transition in Northeastern Svalbard. In: Descent into the Cryogenian. Precambrian Res. 319, 79–95. https://doi.org/10.1016/j.precamres.2017.12.010.

Halverson, G.P., Maloof, A.C., Schrag, D.P., Dudás, F.Ö., Hurtgen, M., 2007. Stratigraphy and geochemistry of a ca 800 Ma negative carbon isotope interval in northeastern Svalbard. In: Precambrian Chemostratigraphy. Chem. Geol. 237, 5–27. https://doi.org/10.1016/j.chemgeo.2006.06.013.

Halverson, G.P., Wade, B.P., Hurtgen, M.T., Barovich, K.M., 2010. Neoproterozoic chemostratigraphy. In: Precambrian Isotope Stratigraphy. Precambrian Res. 182, 337–350. https://doi.org/10.1016/j.precamres.2010.04.007.

Hay, C.C., Creveling, J.R., Hagen, C.J., Maloof, A.C., Huybers, P., 2019. A library of early Cambrian chemostratigraphic correlations from a reproducible algorithm. Geology 47, 457–460. https://doi.org/10.1130/G46019.1.

Heller, P.L., Angevine, C.L., 1985. Sea-level cycles during the growth of Atlantic-type oceans. Earth Planet. Sci. Lett. 75, 417–426. https://doi.org/10.1016/0012-821X(85)90185-2.

Higgins, J.A., Blättler, C.L., Lundstrom, E.A., Santiago-Ramos, D.P., Akhtar, A.A., Crüger Ahm, A.-S., Bialik, O., Holmden, C., Bradbury, H., Murray, S.T., Swart, P.K., 2018. Mineralogy, early marine diagenesis, and the chemistry of shallow-water carbonate sediments. Geochim. Cosmochim. Acta 220, 512–534. https://doi.org/10.1016/j.gca.2017.09.046.

Hodgin, E.B., 2020. A Reappraisal of Neoproterozoic to early Paleozoic Terrane Provenance from the Iapetan Realm and the Tectonic Implications (Ph.D. thesis). Harvard University.

Hoffman, P.F., Lamothe, K.G., 2019. Seawater-buffered diagenesis, destruction of carbon isotope excursions, and the composition of DIC in Neoproterozoic oceans. Proc. Natl. Acad. Sci. 116, 18874–18879. https://doi.org/10.1073/pnas.1909570116.

Husson, J.M., Higgins, J.A., Maloof, A.C., Schoene, B., 2015a. Ca and Mg isotope constraints on the origin of Earth's deepest δ^{13}C excursion. Geochim. Cosmochim. Acta 37. https://doi.org/10.1016/j.gca.2015.03.012.

Husson, J.M., Linzmeier, B.J., Kitajima, K., Ishida, A., Maloof, A.C., Schoene, B., Peters, S.E., Valley, J.W., 2020. Large isotopic variability at the micron-scale in 'Shuram' excursion carbonates from South Australia. Earth Planet. Sci. Lett. 538, 116211. https://doi.org/10.1016/j.epsl.2020.116211.

Husson, J.M., Maloof, A.C., Schoene, B., 2012. A syn-depositional age for Earth's deepest δ^{13}C excursion required by isotope conglomerate tests. Terra Nova 24, 318–325. https://doi.org/10.1111/j.1365-3121.2012.01067.x.

Husson, J.M., Maloof, A.C., Schoene, B., Chen, C.Y., Higgins, J.A., 2015b. Stratigraphic expression of Earth's deepest δ^{13}C excursion in the Wonoka Formation of South Australia. Am. J. Sci. 315, 1–45. https://doi.org/10.2475/01.2015.01.

Jiang, G., Shi, X., Zhang, S., Wang, Y., Xiao, S., 2011. Stratigraphy and paleogeography of the Ediacaran Doushantuo Formation (ca. 635–551 Ma) in South China. Gondwana Res. 19, 831–849. https://doi.org/10.1016/j.gr.2011.01.006.

Kaufman, A.J., Knoll, A.H., Narbonne, G.M., 1997. Isotopes, ice ages, and terminal Proterozoic earth history. Proc. Natl. Acad. Sci. 94, 6600–6605. https://doi.org/10.1073/pnas.94.13.6600.

Knauth, L.P., Kennedy, M.J., 2009. The late Precambrian greening of the Earth. Nature 460, 728–732. https://doi.org/10.1038/nature08213.

Komar, N., Zeebe, R.E., 2016. Calcium and calcium isotope changes during carbon cycle perturbations at the end-Permian. Paleoceanography 31, 115–130. https://doi.org/10.1002/2015PA002834.

Kominz, M.A., 1984. Oceanic ridge volumes and sea-level change - an error analysis. In: Schlee, J.S. (Ed.), Interregional Unconformities and Hydrocarbon Accumulation. In: AAPG Special Volumes, pp. 109–127.

Kroopnick, P.M., 1985. The distribution of ^{13}C of ΣCO_2 in the world oceans. Deep-Sea Res., A, Oceanogr. Res. Pap. 32, 57–84. https://doi.org/10.1016/0198-0149(85)90017-2.

Kump, L.R., Arthur, M.A., 1999. Interpreting carbon-isotope excursions: carbonates and organic matter. Chem. Geol. 161, 181–198. https://doi.org/10.1016/S0009-2541(99)00086-8.

Laakso, T.A., Schrag, D.P., 2020. The role of authigenic carbonate in Neoproterozoic carbon isotope excursions. Earth Planet. Sci. Lett. 549, 116534. https://doi.org/10.1016/j.epsl.2020.116534.

Lau, K.V., Macdonald, F.A., Maher, K., Payne, J.L., 2017. Uranium isotope evidence for temporary ocean oxygenation in the aftermath of the Sturtian Snowball Earth. Earth Planet. Sci. Lett. 458, 282–292. https://doi.org/10.1016/j.epsl.2016.10.043.

Lazar, B., Erez, J., 1990. Extreme ^{13}C depletions in seawater-derived brines and their implications for the past geochemical carbon cycle. Geology 18, 1191–1194. https://doi.org/10.1130/0091-7613(1990)018<1191:ECDISD>2.3.CO;2.

Le Guerroué, E., Allen, P.A., Cozzi, A., 2006. Parasequence development in the Ediacaran Shuram Formation (Nafun Group, Oman): high-resolution stratigraphic test for primary origin of negative carbon isotopic ratios. Basin Res. 18, 205–219. https://doi.org/10.1111/j.1365-2117.2006.00292.x.

Lee, C., Fike, D.A., Love, G.D., Sessions, A.L., Grotzinger, J.P., Summons, R.E., Fischer, W.W., 2013. Carbon isotopes and lipid biomarkers from organic-rich facies of the Shuram Formation, Sultanate of Oman. Geobiology 11, 406–419. https://doi.org/10.1111/gbi.12045.

Macdonald, F.A., Strauss, J.V., Sperling, E.A., Halverson, G.P., Narbonne, G.M., Johnston, D.T., Kunzmann, M., Schrag, D.P., Higgins, J.A., 2013. The stratigraphic relationship between the Shuram carbon isotope excursion, the oxygenation of Neoproterozoic oceans, and the first appearance of the Ediacara biota and bilaterian trace fossils in northwestern Canada. Chem. Geol. 362, 250–272. https://doi.org/10.1016/j.chemgeo.2013.05.032.

Matthews, J.J., Liu, A.G., Yang, C., McIlroy, D., Levell, B., Condon, D.J., 2020. A chronostratigraphic framework for the rise of the Ediacaran macrobiota: new constraints from mistaken point ecological reserve, Newfoundland. GSA Bull. 133, 612–624. https://doi.org/10.1130/B35646.1.

McFadden, K.A., Huang, J., Chu, X., Jiang, G., Kaufman, A.J., Zhou, C., Yuan, X., Xiao, S., 2008. Pulsed oxidation and biological evolution in the Ediacaran Doushantuo

Formation. Proc. Natl. Acad. Sci 105, 3197–3202. https://doi.org/10.1073/pnas.0708336105.

Melezhik, V.A., Pokrovsky, B.G., Fallick, A.E., Kuznetsov, A.B., Bujakaite, M.I., 2009. Constraints on $^{87}Sr/^{86}Sr$ of late Ediacaran seawater: insight from Siberian high-Sr limestones. J. Geol. Soc. 166, 183–191. https://doi.org/10.1144/0016-76492007-171.

Merdith, A.S., Williams, S.E., Collins, A.S., Tetley, M.G., Mulder, J.A., Blades, M.L., Young, A., Armistead, S.E., Cannon, J., Zahirovic, S., Müller, R.D., 2021. Extending full-plate tectonic models into deep time: linking the Neoproterozoic and the Phanerozoic. Earth-Sci. Rev. 214, 103477. https://doi.org/10.1016/j.earscirev.2020.103477.

Miller, K.G., Kominz, M.A., Browning, J.V., Wright, J.D., Mountain, G.S., Katz, M.E., Sugarman, P.J., Cramer, B.S., Christie-Blick, N., Pekar, S.F., 2005. The Phanerozoic record of global sea-level change. Science 310, 1293–1298. https://doi.org/10.1126/science.1116412.

Moynihan, D.P., Strauss, J.V., Nelson, L.L., Padget, C.D., 2019. Upper Windermere Supergroup and the transition from rifting to continent-margin sedimentation, Nadaleen River area, northern Canadian Cordillera. GSA Bull. 131, 1673–1701. https://doi.org/10.1130/B32039.1.

Müller, R.D., Sdrolias, M., Gaina, C., Steinberger, B., Heine, C., 2008. Long-term sea-level fluctuations driven by ocean basin dynamics. Science 319, 1357–1362. https://doi.org/10.1126/science.1151540.

Osburn, M.R., Owens, J., Bergmann, K.D., Lyons, T.W., Grotzinger, J.P., 2015. Dynamic changes in sulfate sulfur isotopes preceding the Ediacaran Shuram Excursion. Geochim. Cosmochim. Acta 170, 204–224. https://doi.org/10.1016/j.gca.2015.07.039.

Popp, B.N., Laws, E.A., Bidigare, R.R., Dore, J.E., Hanson, K.L., Wakeham, S.G., 1998. Effect of phytoplankton cell geometry on carbon isotopic fractionation. Geochim. Cosmochim. Acta 62, 69–77. https://doi.org/10.1016/S0016-7037(97)00333-5.

Rooney, A.D., Cantine, M.D., Bergmann, K.D., Gómez-Pérez, I., Baloushi, B.A., Boag, T.H., Busch, J.F., Sperling, E.A., Strauss, J.V., 2020. Calibrating the coevolution of Ediacaran life and environment. Proc. Natl. Acad. Sci. 117. https://doi.org/10.1073/pnas.2002918117.

Rothman, D.H., Hayes, J.M., Summons, R.E., 2003. Dynamics of the Neoproterozoic carbon cycle. Proc. Natl. Acad. Sci. 100, 8124–8129. https://doi.org/10.1073/pnas.0832439100.

Rowan, M.G., Hearon IV, T.E., Kernen, R.A., Giles, K.A., Gannaway-Dalton, C.E., Williams, N.J., Fiduk, J.C., Lawton, T.F., Hannah, P.T., Fischer, M.P., 2020. A review of allochthonous salt tectonics in the Flinders and Willouran ranges, South Australia. Aust. J. Earth Sci. 67, 787–813. https://doi.org/10.1080/08120099.2018.1553063.

Sarmiento, J.L., Gruber, N., 2006. Ocean Biogeochemical Dynamics. Princeton University Press.

Schrag, D.P., Higgins, John.A., Macdonald, F.A., Johnston, D.T., 2013. Authigenic carbonate and the history of the global carbon cycle. Science 339, 540–543. https://doi.org/10.1126/science.1229578.

Skulan, J., DePaolo, D.J., Owens, T.L., 1997. Biological control of calcium isotopic abundances in the global calcium cycle. Geochim. Cosmochim. Acta 61, 2505–2510. https://doi.org/10.1016/S0016-7037(97)00047-1.

Stiller, M., Rounick, J.S., Shasha, S., 1985. Extreme carbon-isotope enrichments in evaporating brines. Nature 316, 434–435. https://doi.org/10.1038/316434a0.

Strauss, J.V., MacDonald, F.A., Halverson, G.P., Tosca, N.J., Schrag, D.P., Knoll, A.H., 2015. Stratigraphic evolution of the Neoproterozoic Callison Lake Formation: linking the break-up of Rodinia to the Islay carbon isotope excursion. Am. J. Sci. 315, 881–944. https://doi.org/10.2475/10.2015.01.

Strauss, J.V., Tosca, N.J., 2020. Mineralogical constraints on Neoproterozoic pCO2 and marine carbonate chemistry. Geology 48, 599–603. https://doi.org/10.1130/G47506.1.

Summa, C.L., 1993. Sedimentologic, stratigraphic, and tectonic controls of a mixed carbonate-siliciclastic succession; Neoproterozoic Johnnie Formation, Southeast California (Ph.D. thesis). Massachusetts Institute of Technology, Cambridge, MA.

Tanczyk, E.I., Lapointe, P., Morris, W.A., Schmidt, P.W., 1987. A paleomagnetic study of the layered mafic intrusion at Sept-Îles, Quebec. Can. J. Earth Sci. 24, 1431–1438. https://doi.org/10.1139/e87-135.

Tang, J., Dietzel, M., Böhm, F., Köhler, S.J., Eisenhauer, A., 2008. Sr^{2+}/Ca^{2+} and $^{44}Ca/^{40}Ca$ fractionation during inorganic calcite formation: II. Ca isotopes. Geochim. Cosmochim. Acta 72, 3733–3745. https://doi.org/10.1016/j.gca.2008.05.033.

van Staal, C., Chew, D., Zagorevski, A., McNicoll, V., Hibbard, J., Skulski, T., Castonguay, S., Escayola, M., Sylvester, P., 2013. Evidence of late Ediacaran hyperextension of the Laurentian Iapetan Margin in the Birchy Complex, Baie Verte Peninsula, Northwest Newfoundland: implications for the opening of Iapetus, Formation of peri-Laurentian microcontinents and taconic – Grampian orogenesis. Geosci. Can. 40, 94–117. https://doi.org/10.12789/geocanj.2013.40.006.

Verdel, C., Niemi, N., van der Pluijm, B.A., 2011. Variations in the Illite to muscovite transition related to metamorphic conditions and detrital muscovite content: insight from the Paleozoic passive margin of the Southwestern United States. J. Geol. 119, 419–437. https://doi.org/10.1086/660086.

Watts, A.B., 1982. Tectonic subsidence, flexure and global changes of sea level. Nature 297, 469–474. https://doi.org/10.1038/297469a0.

Yang, C., Rooney, A.D., Condon, D.J., Li, X.-H., Grazhdankin, D.V., Bowyer, F.T., Hu, C., Macdonald, F.A., Zhu, M., 2021. The tempo of Ediacaran evolution. Sci. Adv. 7, eabi9643. https://doi.org/10.1126/sciadv.abi9643.

Youbi, N., Ernst, R.E., Söderlund, U., Boumehdi, M.A., Lahna, A.A., Tassinari, C.C.G., Moume, W.E., Bensalah, M.K., 2020. The Central Iapetus magmatic province: an updated review and link with the ca. 580 Ma Gaskiers glaciation. Geol. Soc. Am., Spec. Pap. 544, 35–66. https://doi.org/10.1130/2020.2544(02).